nature geoscience

Article

https://doi.org/10.1038/s41561-024-01498-y

Moist heatwaves intensified by entrainment of dry air that limits deep convection

Received: 6 January 2024

Accepted: 28 June 2024

Published online: 25 July 2024

Check for updates

Suqin Q. Duan [®] ⊠, Fiaz Ahmed & J. David Neelin

Moist heatwaves in the tropics and subtropics pose substantial risks to society, yet the dynamics governing their intensity are not fully understood. The onset of deep convection arising from hot, moist near-surface air has been thought to limit the magnitude of moist heatwayes. Here we use reanalysis data, output from the Coupled Model Intercomparison Project Phase 6 and model entrainment perturbation experiments to show that entrainment of unsaturated air in the lower-free troposphere (roughly 1–3 km above the surface) limits deep convection, thereby allowing much higher near-surface moist heat. Regions with large-scale subsidence and a dry lower-free troposphere, such as coastal areas adjacent to hot and arid land, are thus particularly susceptible to moist heatwaves. Even in convective regions such as the northern Indian Plain, Southeast Asia and interior South America, the lower-free tropospheric dryness strongly affects the maximum surface wet-bulb temperature. As the climate warms, the dryness (relative to saturation) of the lower-free tropospheric air increases and this allows for a larger increase of extreme moist heat, further elevating the likelihood of moist heatwaves.

Moist heat, encompassing the combined stress of temperature and humidity on human physiology, is especially pertinent to human health: high moist heat interferes with the body's ability to dissipate metabolic heat and maintain a normal core temperature, leading to hyperthermia and even heat death¹⁻⁵. The high physiological strain during moist heatwaves can aggravate the risks of cardiovascular and respiratory diseases^{6,7}, reduce the physical work capacity of outdoor workers^{8,9} and increase heat-related hospitality and mortality^{10,11}, substantially affecting societal health and economic welfare^{12–14}. Being warm, moist and densely populated, the tropics and subtropics have the largest potential exposure to moist heatwaves and are projected to have the most pronounced enhancement of exposure as climate warms^{15–19}. It is therefore crucial to understand the environmental control of the magnitude and spatial distribution of moist heatwaves in these tropical and subtropical regions.

There are a suite of indices to measure moist heat $^{20-22}$. The wet-bulb temperature (WBT) has been widely used in the past decade, especially when discussing the physical climate conditions associated the extreme moist heat $^{1,16,19,23-26}$. WBT is closely related with moist enthalpy $^{27-29}$ and also with moist static energy (MSE) (Methods) provided the orographic

height is modest (which is typical for places with high moist heat). Fortunately, boundary-layer MSE in the tropics is constrained by tropical convection and dynamics $^{30-36}$ and, in some circumstances, may set an upper limit on the magnitude of moist heat.

Recent studies have employed theories of tropical convection and dynamics to understand the constraint on moist heat extremes 25,29 and temperature extremes ^{37–39}. The fundamental ingredients that form the constraint are: (1) convective quasi-equilibrium (QE)^{30,31}, which states that convecting atmospheres are close to being neutrally buoyant and (2) The weak temperature gradient (WTG) approximation^{33,40}, which states that tropical free-tropospheric temperatures are close to being spatially uniform, particularly along the zonal direction. Quantitatively, QE can be expressed in an idealized form as $MSE_{2m} = MSE_{500}^*$, where MSE_{2m} is the near-surface MSE and MSE_{500}^* is the saturated MSE at 500 hPa. When MSE_{2m} exceeds MSE_{500}^* , the boundary layer becomes unstable, resulting in deep convection and limiting further increases in MSE_{2m}. The WTG approximation implies that the local MSE^{*}₅₀₀ value (which is a function of temperature alone) is approximately equal to its zonal-mean value ($(MSE_{500}^*)_{7M}$). Together, the QE and WTG conditions imply that $(MSE_{500}^*)_{7M}$ provides a constraint on MSE_{2m} , and

Department of Atmospheric and Oceanic Sciences, University of California, Los Angeles, Los Angeles, CA, USA. 🖂 e-mail: sqduan@ucla.edu

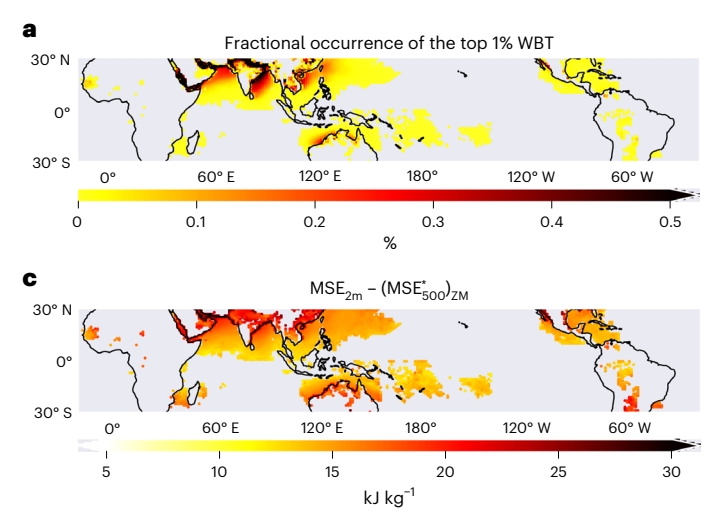
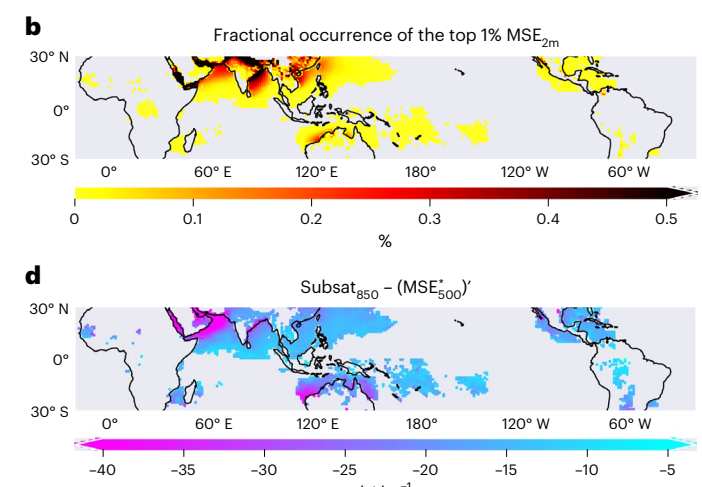


Fig. 1 | Spatial distribution of extreme moist heat days and the associated convective conditions. a, The location and fractional occurrences (colour) of the top 1% daily mean WBT sampled, respectively, for land, ocean and coast. The fractional occurrence is defined as the number of occurrences of the spatiotemporally sampled top 1% days at each location to the total number of the spatio-temporally sampled top 1% days. Locations without days in the top 1% are masked and not coloured. b, The location and fractional occurrences of the top



1% daily mean MSE at the reference height (MSE $_{2m}$) sampled, respectively, for land, ocean and coast. $\mathbf{c.d.}$ The corresponding boundary-layer instability measure (\mathbf{c}), defined as the deviation of MSE $_{2m}$ from the zonal-mean saturated MSE at 500 hPa ((MSE $_{500}^*)_{ZM}$) and lower-free tropospheric dryness measure (\mathbf{d}), defined as the subsaturation at 850 hPa (Subsat $_{850}$) minus the local MSE $_{500}^*$ anomalies from the zonal-mean value ((MSE $_{500}^*)'$), of these top 1% WBT days. See Methods for details of the sampling method and the calculation of each quantity.

thereby a constraint on near-surface moist heat. Local moist heat extremes in the tropics, regardless of the heterogeneous local surface and meteorological conditions, will need to behave under the constraint of $(MSE_{500}^*)_{7M}$.

The line of argument presented above neglects the limiting impacts of free-tropospheric dry air entrainment on convection $^{41-44}$. We demonstrate that dry air aloft (in the lower-free troposphere (LFT)) has a substantial effect on the magnitude and occurrence of surface moist heat extremes. Lower-free tropospheric dry air curtails convection, allowing the build-up of greater boundary-layer instability. This pushes MSE_{2m} to greater extremes than would otherwise be encountered. Accounting for dry air entrainment also explains why extreme WBT values can occur in both climatologically precipitating and non-precipitating tropical regions (for example, the Red Sea and the Persian Gulf in Fig. 1a) where convective QE will not hold.

Extreme moist heat spatial distribution in current climate

The tight link between surface WBT and MSE_{2m} extremes is illustrated in Fig. 1a,b. Extreme WBT occurs where MSE_{2m} is high. Over land, extreme moist heat occurs over northern India, Southeast and East Asia, interior South America and west and central Africa, consistent with observational findings 19,45. Over oceans, these high moist heat days are found over the West Pacific Warm Pool, the Bay of Bengal, the Arabian Sea and the equatorial South Pacific. These land and oceanic regions are warm, humid and typically having active deep convection. In addition, coastal regions adjacent to hot and dry land are also hot spots of the extreme moist heat days such as the Red Sea, the Persian Gulf, the gulfs of California and Mexico, and seas around northern Australia and Madagascar.

The top 1% WBT days correspond to times when the boundary layer is highly unstable (Fig. 1c), where the instability is measured by the exceedance of MSE_{2m} over $(\mathsf{MSE}_{500}^*)_{ZM}$. The large MSE_{2m} exceedance tends to be accompanied by relatively large magnitudes of LFT subsaturation (Fig. 1d). Here, LFT subsaturation is the saturation deficit at 850 hPa—a measure of the tropospheric dryness (Methods). Regions with both high MSE_{2m} and large LFT subsaturation are home to the most extreme moist heat cases. We discuss in more detail the

relationship between the MSE_{2m} exceedance and the LFT subsaturation below.

More extreme moist heat under entraining QE

We incorporate the LFT dry air effects to the QE–WTG framework and consider an 'entraining QE'. We use the LFT subsaturation (Subsat_850) to represent the integrated properties of LFT entrained air. Empirical evidence suggests that a buoyancy measure that incorporates this LFT subsaturation is a strong indicator of tropical convective activity $^{44,46-48}$. By considering the entrainment effect and keeping a term representing the deviations from WTG (which is small compared with the entrainment term) (see Methods for further details) entraining QE–WTG can be represented by:

$$(MSE_{2m} - (MSE_{500})_{ZM})$$
boundary – layer instability measure
$$+(w Subsat_{850} - (MSE_{500}^*)') = 0.$$
LFT dryness measure

The relative contribution of the boundary-layer instability and LFT dryness to convective buoyancy depends on the weighting w of LFT environmental air typically entrained by convecting plumes. Observations suggest that both the boundary layer and LFT contribute nearly equally to the properties of a convective plume 44,46,49 , yielding approximately equal weighting 47 of the instability and dryness measures, that is, $w \approx 1$ in equation (1). Climate models with slightly different entrainment could have slightly different values of w, but the overall effects would be similar.

Figure 2 shows the joint frequency distribution of boundary-layer instability and LFT subsaturation measures that appear in equation (1). This figure format allows us to evaluate extreme moist heat incidence in relation to the idealized QE–WTG theory, and the crucial role of LFT entrainment. The green and brown shadings show the frequency of raining and non-raining days, respectively. The boundary-layer instability measures the buoyancy of a non-entraining convective plume. Under idealized (non-entraining) QE, this measure should be either around zero (neutrally buoyant convection; purple line in Fig. 2) or negative

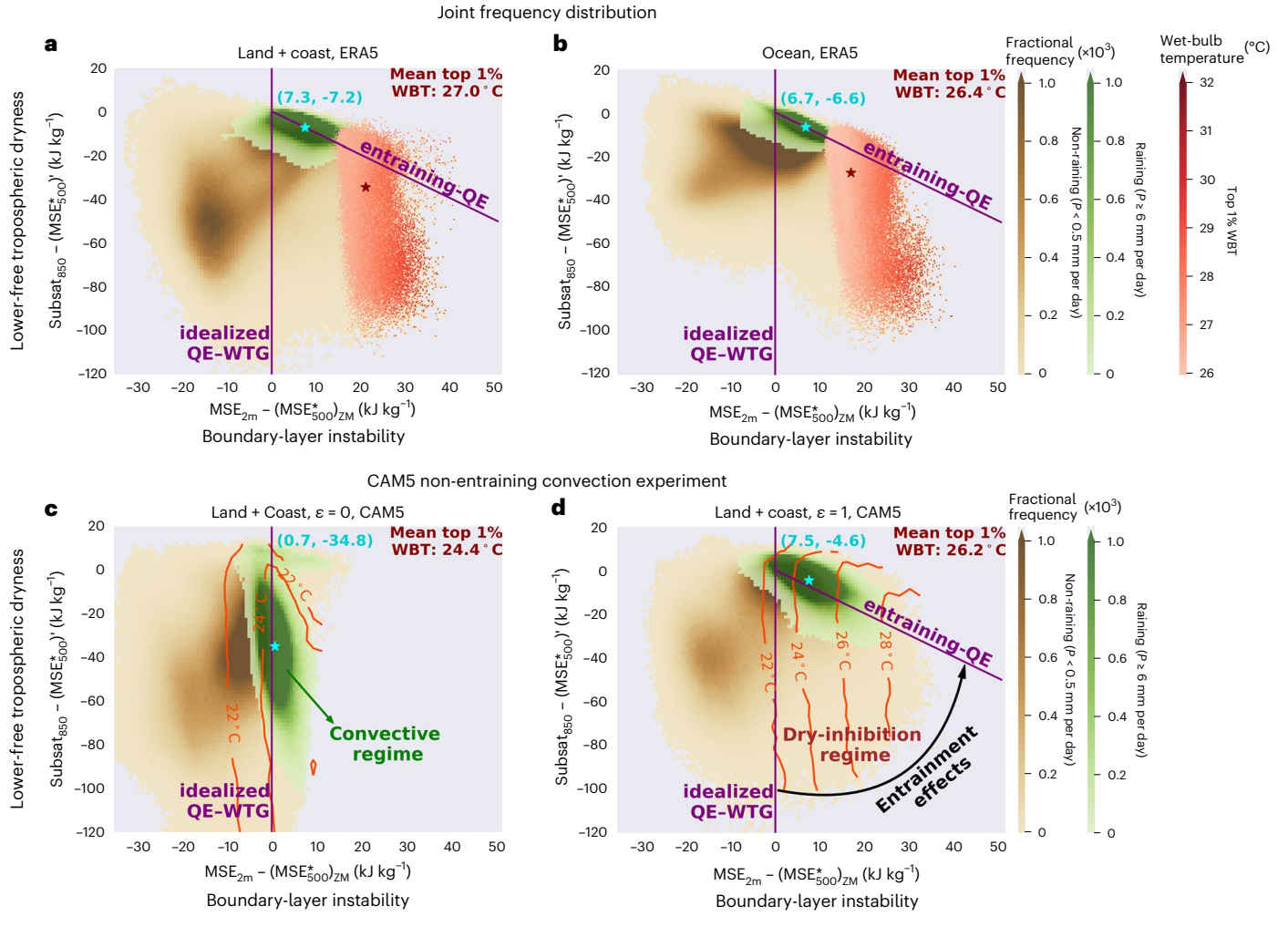


Fig. 2 | The joint frequency distribution between boundary-layer instability and lower-free tropospheric dryness measures, and its relationship to extreme WBTs. a,b, The frequency of non-raining (daily mean precipitation rate P < 0.5 mm per day; brown shadings) and raining ($P \ge 6$ mm per day; green shadings) conditions, and the top 1% WBT days (red dots) as a function of the two measures, for land plus coast (a) and ocean (b) in ERAS. The corresponding distribution that only include grid cells over land is shown in Extended Data Fig. 1. The vertical purple line marks the position of value zero on the x axis, where a combination of idealized theories of QE and WTG sets the constraint for

 $\mathsf{MSE}_{2m}.$ The slanted purple line is the 1:–1 line of the boundary-layer instability measure and the lower-free tropospheric dryness measure which we refer to as the 'entraining QE' line. The cyan stars show the mean of the two measures (values denoted in the parentheses) for raining conditions. The dark red stars show the mean of the two measures for the top 1% WBT days. \mathbf{c},\mathbf{d} , The joint frequency distribution for land plus coast in CAM5 runs; from runs without entrainment (\mathbf{c}) and with standard entrainment (\mathbf{d}). The orange lines show the bin-maximum WBTs, indicating conditions where these WBT values start to occur. The WBT value averaged over the 1% WBT days is given at the upper right corner.

(stable to deep convection). However, in realistic situations, both over land plus coast (Fig. 2a) and over ocean (Fig. 2b), a large number of samples in non-raining conditions and almost all samples in raining conditions lie to the right of the purple line. The occurrence of large $\text{MSE}_{2m}^*\text{exceedance}$ over $(\text{MSE}_{500}^*)_{ZM}$ is explained after incorporating the effects of LFT entrainment as in equation (1).

The LFT dryness dilutes the initial MSE of the boundary-layer air as it ascends through the troposphere. Higher MSE_{2m} values can therefore be attained without triggering convection. The slanted purple line in Fig. 2 is the 'entraining QE line', illustrated as 1:–1 (w=1 in equation (1)). Conditions around this line are in a state of neutral entraining buoyancy, where the boundary-layer instability perfectly compensates for the LFT entrainment effect. The entraining QE line shifts the upper bound on MSE_{2m} (or moist heat) to larger values, because conditions that are unstable by the non-entraining measure can now be stable by the new measure that incorporates entrainment. The raining samples (green shading), instead of following the non-entraining QE limit, align along this entraining QE line. These raining samples represent the convective regime of the high MSE_{2m} cases. The mean values of ERA5 MSE_{2m}

exceedance and the entrainment effect for the convective regime are around 7 kJ kg⁻¹ for both land plus coast and ocean (Fig. 2a,b, cyan stars). In addition to the convective regime, shifting the idealized QE line to this entraining QE line also permits the existence of a wedge-shaped non-raining 'dry-inhibition regime'. In this regime, the boundary layer is warm and moist (high MSE_{2m} exceedance), but the LFT is too dry to foster deep convection (Fig. 2d).

To illustrate where extreme moist heat days occur, we show the top 1% WBT days in Fig. 2a,b as the red dots: they coincide with times having the highest boundary-layer instability values. All these top 1% WBT days exceed the MSE $_{\rm 2m}$ bound placed by an idealized, non-entraining QE constraint. More detailed correspondence of WBT values to the magnitude of this exceedance is shown in Extended Data Fig. 2. The top 1% WBT days—the averages of them are marked by a dark red star with a mean intensity of about 27 °C—lie either in the convective regime or the dry-inhibition regime. Days with moderate LFT subsaturation tend to lie around the entraining QE line and are more likely to be raining. Days with larger LFT subsaturation tend to lie within the dry-inhibition regime; these days accumulate large values of boundary-layer MSE

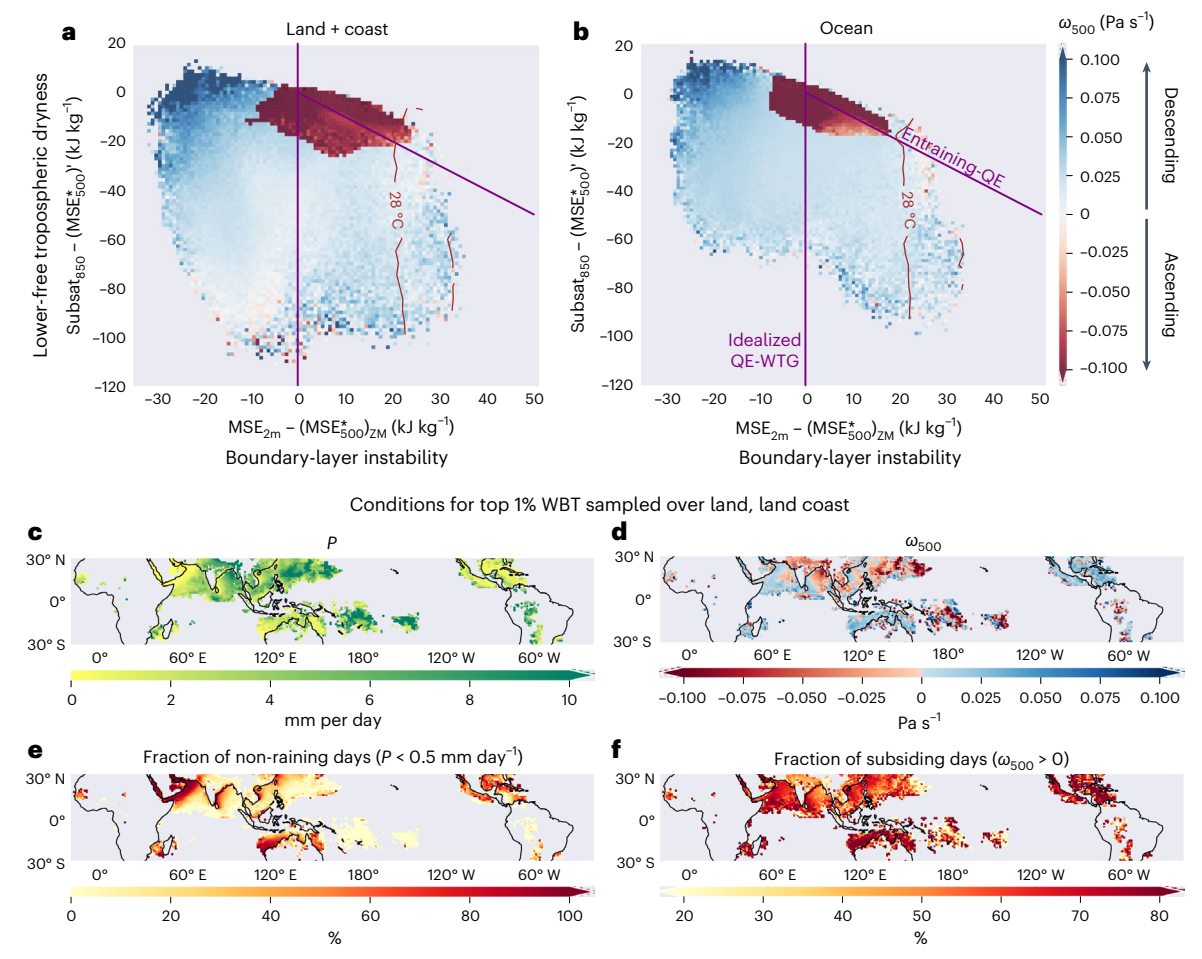


Fig. 3 | Large-scale dynamical conditions of the convective regime, the dry-inhibition regime and days with extreme WBT values. a,b, Vertical velocity at 500 hPa (ω_{500} , averaged in each conditional bin) corresponding to Fig. 2a,b; negative values represent ascending motion and are coloured red while positive values represent descending motion and coloured blue. The bins with counts less than 3 are masked. The thin red lines mark the bin-maximum WBTs of 28 °C and 30 °C, indicating conditions where these health-threatening WBT

days start to occur. \mathbf{c} - \mathbf{f} , The conditional mean precipitation rate (P) (\mathbf{c}), ω_{500} (\mathbf{d}), fraction of non-raining days (P < 0.5 mm per day) (\mathbf{e}) and fraction of days with downward motion at 500 hpa (ω_{500} > 0) (\mathbf{f}) for the top 1% WBT days. The sampling of \mathbf{c} - \mathbf{f} is the same as in Fig. 1a,c,d, where the top 1% WBT days are sampled spatio-temporally and respectively over land, ocean and coast. Data are from ERAS (ref. 69).

but do not reach the convective, entraining QE state on account of excessive LFT dryness.

The impacts of entrainment on moist heat extreme magnitudes is further verified using a parameter perturbation experiment with version 5 of the Community Atmospheric Model (CAM5)⁵⁰. A control run with standard entrainment and a non-entraining run with zero entrainment are used (Methods). The joint frequency distribution over land plus coast for the non-entraining and the default entraining cases are shown in Fig. 2c,d. Without entrainment, the idealized, non-entraining QE-WTG line restricts the MSE_{2m} values in both raining and non-raining conditions. In particular, the raining conditions lie close to a state of non-entraining QE. With entrainment, a substantial number of samples under both raining and non-raining conditions exceed the idealized QE limit. The raining days align along the entraining QE line, while the non-raining days are situated in the dry-inhibition regime-similar to the reanalysis data (Fig. 2a). WBTs in the entraining and non-entraining runs indeed differ (orange contours): the run with entrainment exhibits higher WBT values, with the top 1% days having a mean WBT value of 26.2 °C, in contrast to 24.4 °C in the non-entraining run.

The entraining QE and the dry-inhibition regimes exist under different large-scale conditions. Figure 3a,b shows the corresponding vertical velocity at 500 hPa (ω_{500}): the convective regime is in ascending motion and the dry-inhibition regime, on average, experiences

subsiding motion. This subsidence, whether transient or seasonal, contributes to maintaining the LFT dryness within the dry-inhibition regime $^{\rm SI}$. Some of the highest surface WBT values (see the dark red WBT contours of 28 °C and 30 °C) occur within this regime.

The regional precipitation condition and vertical motion of extreme moist heat days are shown in Fig. 3c–f. The top 1% WBT days over the northern India Plain, Southeast Asia, South America, West Pacific Warm Pool and tropical South Pacific are in the deep-convective regime: the fraction of non-raining days is low (Fig. 3e), conditional mean P is high (Fig. 3c) and ω_{500} is on average upward (Fig. 3d,f). Extreme moist heat days in these regions lie around the entraining QE line in Fig. 2a,b. By contrast, the top 1% WBT days over those coastal oceans adjacent to hot and arid land are in the subsiding dry-inhibition regime: the fraction of non-raining days is high and ω_{500} is on average downward. These extreme moist heat days constitute the long tail of red dots that have large LFT subsaturation in Fig. 2a,b.

Faster increase of the extreme moist heat under warming

We now examine how entraining QE and its relations with the extreme WBT days change in a warmer climate. We compare simulations under the $4\times$ CO $_2$ and the base climate states using climate model output from Phase 6 of the Coupled Model Intercomparison Project

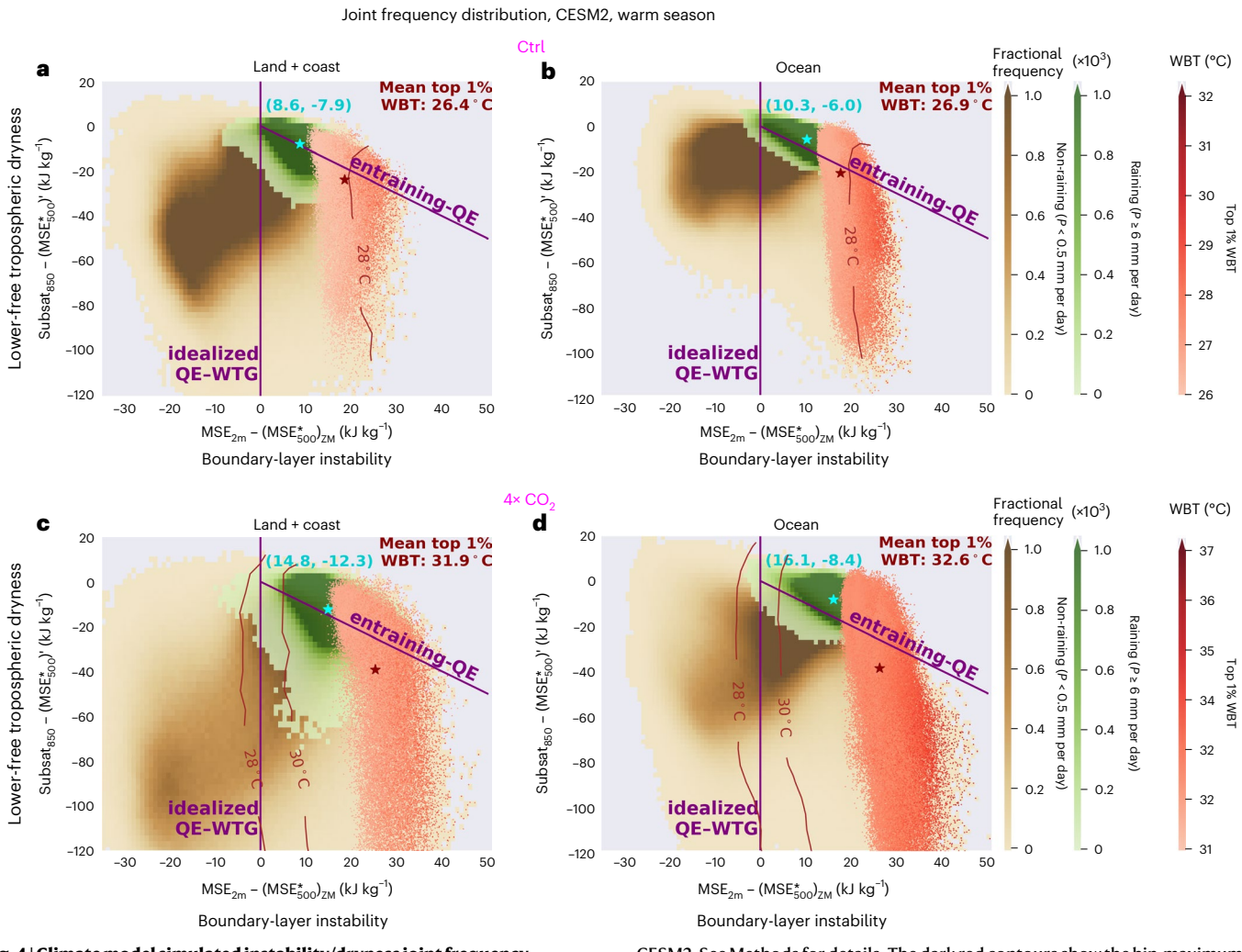


Fig. 4 | Climate model simulated instability/dryness joint frequency distribution and extreme moist heat days. a-d, Similar to Fig. 2, but with the results from the base climate state (Ctrl) for land plus coast (a) and ocean (b) and the results from the $4 \times CO_2$ climate state for land plus coast (c) and ocean (d) in

CESM2. See Methods for details. The dark red contours show the bin-maximum WBT of $28\,^{\circ}$ C and $30\,^{\circ}$ C, marking conditions where these health threatening WBT days start to occur.

(CMIP6) 52 . Figure 4 displays the joint frequency distribution of the instability/dryness measures, overlaid with the top 1% WBT days (red dots)—as in Fig. 2a,b but from Community Earth System Model Version 2 (CESM2) 53 simulations. In both the base (Fig. 4a,b) and the 4× CO $_2$ (Fig. 4c,d) climate states, the top 1% WBT days exceed the idealized non-entraining constraint by tens of kJ per kg. The base-state joint distribution simulated by CESM2 is similar to that in ERA5. Multiple other CMIP6 models also show qualitatively similar patterns (Extended Data Fig. 3).

As climate warms, two factors affect the extreme WBT values. First, an overall thermodynamic increase of MSE_{2m} with warming resulting from the increase of surface air temperature and the increase of specific humidity due to the Clausius–Clapeyron effect^{39,54–57}. This thermodynamic increase of MSE_{2m} , by the traditional reasoning of idealized QE–WTG, changes with $(MSE_{500}^*)_{ZM}^{25,37,38,58}$. Second, which we highlight, an excessive increase of extreme MSE_{2m} beyond the increase of $(MSE_{500}^*)_{ZM}$. In CESM2, the mean MSE_{2m} exceedance in raining conditions increases from about 9 kJ kg $^{-1}$ in the base climate to about 15 kJ kg $^{-1}$ in the $4 \times CO_2$ climate over land plus coast. Similar increases are observed over the ocean. This higher MSE_{2m} exceedance in a warmer climate is accompanied by more subsaturated LFT. For instance, the mean raining LFT subsaturation over land plus coast changes from about -8 to -12 kJ kg $^{-1}$. The projected increases in tropospheric dryness

under global warming^{54,59} thus can play an important role in setting the magnitude of surface WBT extremes in a warmer climate.

In the CESM2 warm season, the top 1% WBT days have a mean WBT value of about 26 °C over land, 27 °C over coast and 27 °C over ocean in the base climate. These values increase to about 32 °C, 33 °C and 33 °C in the 4×CO₂ climate. The average rate of the top 1% WBT increase per degree tropical mean warming is 0.9 °C °C⁻¹. These top 1% WBT days encompass an ambient dry bulb temperature of 27-40 °C and a relative humidity of 30-95%. According to the results from physiological experiments^{60,61} and a physiology-based heat index model^{5,62}, under these conditions, human core temperature would start to rise at a WBT of 26-30 °C (the exact value can vary for different metabolic rates and other environmental conditions such as the wind speed). A WBT higher than 31 °C is rarely observed in the current climate, and a WBT beyond 28 °C is among the highest observed values 1,17,19,45. Here, in Fig. 4, we mark the conditional bin-maximum WBT values of 28 °C and 30 °C with dark red contours to indicate where these health-threatening WBT start to occur. Not surprisingly, as climate warms, the distribution surpasses these contours much more frequently. This increased frequency of health-threatening moist heatwave days coincides with increases in the range of boundary-layer instability and LFT dryness measures.

Figure 5a,b shows the multi-model mean changes in the joint frequency distribution between the two climate states (changes for

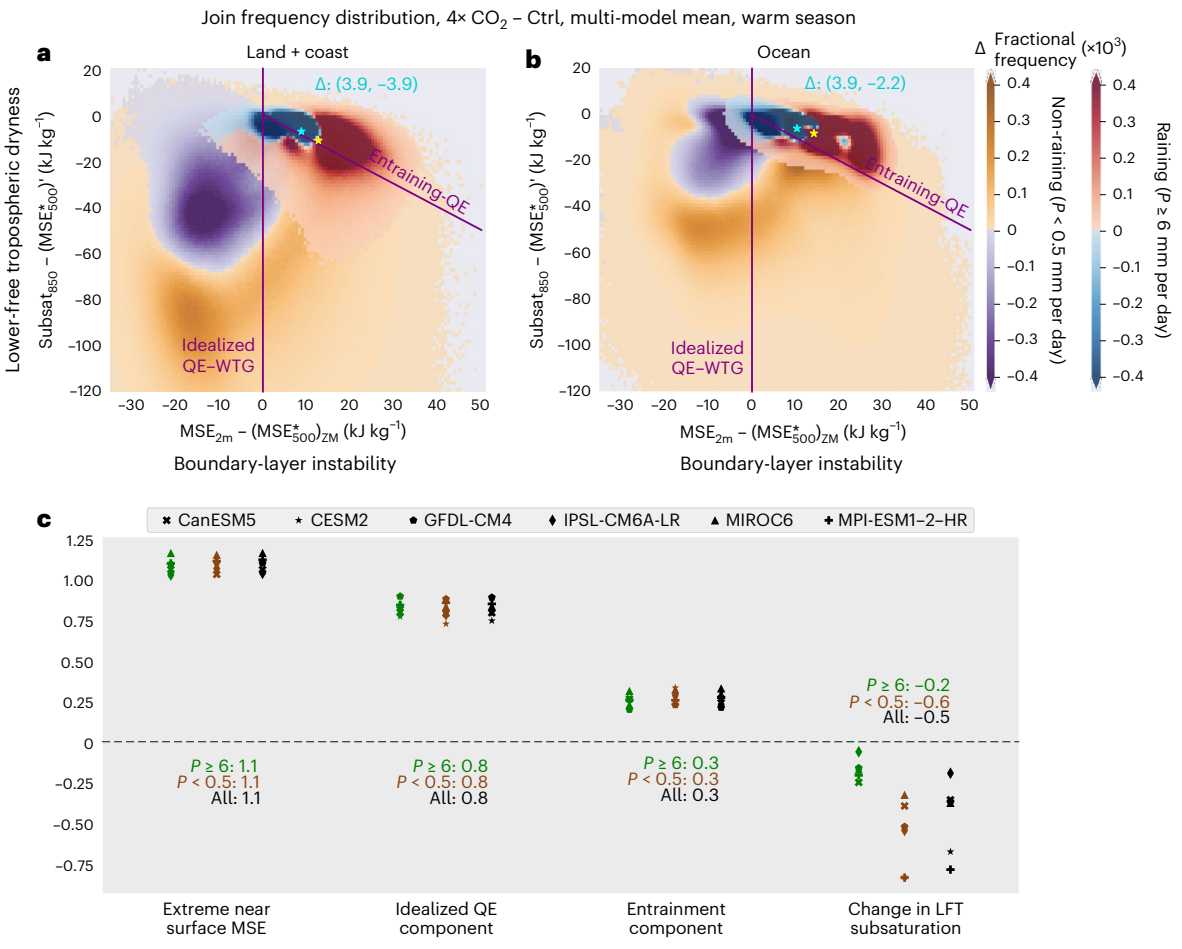


Fig. 5 | Changes in the joint frequency distribution of the instability/dryness measures, and decomposing the increases in extreme MSE_{2m}, a,b, Multi-model mean changes in the joint instability/dryness frequency distribution between the $4 \times \text{CO}_2$ and the base climate states, for non-raining (daily mean precipitation rate P < 0.5 mm per day; orange/purple shadings) and raining conditions ($P \ge 6$ mm per day; red/blue shadings) over land and coast (a) and over ocean (b). The frequency distributions are averaged across models first before contrasting between the two climate states. The small non-contiguous blue area within the red shading in b is mainly contributed by one individual model CanESM5. The cyan and the yellow stars mark the mean values of the two measures averaged

over raining conditions in the base (cyan) and the warm (yellow) climate; the cyan texts aside denote the magnitude of changes in these mean values. \mathbf{c} , Decomposing the scaling of the top 1% MSE $_{2m}$ into the 'idealized QE component' $\Delta (\text{MSE}_{500}^*)_{ZM}$ and the 'entrainment component' $\Delta (\text{MSE}_{2m} - (\text{MSE}_{500}^*)_{ZM})$. Also shown is the change of the LFT dryness measure; all terms are conditioned on the top 1% MSE $_{2m}$ days and normalized by the mean change of MSE $_{2m}$ during raining conditions (P > 6 mm per day). Each symbol represents an individual model and the colours separate the scaling for raining (green), non-raining (brown) and all (black) conditions. Numbers denoted are values averaged over models.

individual models are similar; Extended Data Fig. 4). For raining conditions, the distribution shifts approximately along the entraining QE line, towards a more subsaturated LFT and a higher exceedance of MSE_{2m} beyond the $(\mathsf{MSE}_{500}^*)_{ZM}$ constraint. This indicates that the convective regime follows a similar entraining QE in a warmer climate. For the non-raining conditions, LFT becomes even more subsaturated.

Figure 5c breaks down the rate of change in the extreme (top 1%) MSE_{2m} into the 'idealized QE component', that is, increases in $(MSE_{500}^*)_{ZM}$ and the 'entrainment component', namely, increases in the MSE_{2m} exceedance. Also shown is the change in LFT subsaturation. The increase of extreme MSE_{2m} scales with the mean precipitating MSE_{2m} (ref. 36) by a factor of 1.1, and similar for both raining and non-raining conditions. This indicates that extreme MSE_{2m} (thereby extreme moist heat) increases at a similar but faster rate than the precipitating MSE_{2m} . The idealized QE component increases by 0.8 kJ kg⁻¹ and the entrainment component by 0.3 kJ kg⁻¹ per unit kJ kg⁻¹ change in mean precipitating MSE_{2m} , contributing to increases in the extreme MSE_{2m} by about 73% and 27%, respectively. For raining conditions, increases in LFT subsaturation approximately compensates increases in the entrainment component. For non-precipitating conditions, the LFT is so dry (subsaturated) that

convection cannot develop. In the absence of convection and away from entraining QE, the LFT subsaturation need not compensate for increases in boundary-layer instability. The enhancement in LFT subsaturation under non-raining conditions correspondingly has a larger magnitude and a larger spread across models.

Outlook: importance of the LFT for moist heat assessment

Moist heatwaves, characterized by high near-surface temperature and humidity, is particularly relevant to human health. Due to its tight connection to surface MSE, the onset of deep moist convection might limit the upper values of WBT. The entrainment of dry air above the surface can inhibit the onset of deep convection even when the boundary layer is unstable from the strict QE perspective. Here, we show that this entrainment effect increases the convective limit for the magnitude of moist heat. Varying the entrainment rate from zero to a default value in CAM5 can lead to simulated extreme WBTs be higher by about 2°. Moreover, this entrainment effect also allows for a large number of the extreme moist heat cases to occur in a dry-inhibition regime with subsiding motion and suppressed convection. Consequently, extreme

moist heatwaves are not only found in regions that are typically warm, humid and with active convection, but also in regions that have a dry LFT and a warm, moist boundary layer. Coastal areas adjacent to hot and arid land are therefore particularly susceptible to extreme moist heatwaves. As climate warms, the saturation deficit of the LFT increases, resulting in further increase in the intensity of moist heat beyond the overall thermodynamic warming effect. Many of these hot spot regions are densely populated, making it particularly urgent to understand the physics and dynamics of moist heatwaves.

Global climate models and the ERA5 reanalysis simulate qualitatively similar distributions of the instability and dryness measures and extreme moist heat values in relation to them. Nevertheless, the entrainment perturbation experiment in CAM5 shows that the entrainment parameter within the model convection scheme can affect the simulated magnitude of the two measures, extent of the convective and dry-inhibition regimes, and the intensity of moist heat. One degree difference in moist heatwave intensity may indicate billions of person-hours exposed to health-threatening conditions^{63,64}. Yet this aspect of convective physics is highly parameterized in standard global climate models. The results here imply that validation of the lower-free tropospheric simulation is important for assessing projections of surface moist heatwaves. Process-oriented diagnostics to constrain entrainment in climate models^{48,65-67} and risk assessment using storm-resolving simulations⁶⁸ are two avenues to reducing uncertainties. In both, the instability-dryness joint distribution presented in this study provides a useful framework for improving confidence in projections of moist heatwave occurrence and intensity.

Online content

Any methods, additional references, Nature Portfolio reporting summaries, source data, extended data, supplementary information, acknowledgements, peer review information; details of author contributions and competing interests; and statements of data and code availability are available at https://doi.org/10.1038/s41561-024-01498-y.

References

- Sherwood, S. C. & Huber, M. An adaptability limit to climate change due to heat stress. Proc. Natl Acad. Sci. USA 107, 9552–9555 (2010).
- Hanna, E. G. & Tait, P. W. Limitations to thermoregulation and acclimatization challenge human adaptation to global warming. Int. J. Environ. Res. Public Health 12, 8034–8074 (2015).
- 3. Buzan, J. R. & Huber, M. Moist heat stress on a hotter Earth. *Ann. Rev. Earth Planet. Sci.* **48**, 623–655 (2020).
- Cottle, R. M., Lichter, Z. S., Vecellio, D. J., Wolf, S. T. & Kenney, W. L. Core temperature responses to compensable versus uncompensable heat stress in young adults (PSU HEAT Project). J. Appl. Physiol. 133, 1011–1018 (2022).
- Lu, Y.-C. & Romps, D. M. Predicting fatal heat and humidity using the heat index model. J. Appl. Physiol. 134, 649–656 (2023).
- Cheng, J. et al. Cardiorespiratory effects of heatwaves: a systematic review and meta-analysis of global epidemiological evidence. *Environ. Res.* 177, 108610 (2019).
- Khatana, S. A. M., Werner, R. M. & Groeneveld, P. W. Association of extreme heat and cardiovascular mortality in the United States: a county-level longitudinal analysis from 2008 to 2017. *Circulation* 146, 249–261 (2022).
- Foster, J., Hodder, S. G., Lloyd, A. B. & Havenith, G. Individual responses to heat stress: implications for hyperthermia and physical work capacity. Front. Physiol. 11, 541483 (2020).
- Ioannou, L. G. et al. Occupational heat strain in outdoor workers: a comprehensive review and meta-analysis. *Temperature* 9, 67–102 (2022).
- Gasparrini, A. et al. Mortality risk attributable to high and low ambient temperature: a multicountry observational study. *Lancet* 386, 369–375 (2015).

- Liss, A. & Naumova, E. N. Heatwaves and hospitalizations due to hyperthermia in defined climate regions in the conterminous USA. Environ. Monitor. Assess. 191, 1–16 (2019).
- Zander, K. K., Botzen, W. J., Oppermann, E., Kjellstrom, T. & Garnett, S. T. Heat stress causes substantial labour productivity loss in Australia. *Nat. Clim. Change* 5, 647–651 (2015).
- 13. Ebi, K. L. et al. Hot weather and heat extremes: health risks. *Lancet* **398**, 698–708 (2021).
- 14. Borg, M. A. et al. Occupational heat stress and economic burden: a review of global evidence. *Environ. Res.* **195**, 110781 (2021).
- Mora, C. et al. Global risk of deadly heat. Nat. Clim. Change 7, 501–506 (2017).
- Coffel, E. D., Horton, R. M. & De Sherbinin, A. Temperature and humidity based projections of a rapid rise in global heat stress exposure during the 21st century. *Environ. Res. Lett.* 13, 014001 (2017).
- 17. Im, E.-S., Pal, J. S. & Eltahir, E. A. Deadly heat waves projected in the densely populated agricultural regions of South Asia. *Sci. Adv.* **3**, e1603322 (2017).
- Li, D., Yuan, J. & Kopp, R. E. Escalating global exposure to compound heat-humidity extremes with warming. *Environ. Res.* Lett. 15, 064003 (2020).
- Rogers, C. D. et al. Recent increases in exposure to extreme humid-heat events disproportionately affect populated regions. Geophys. Res. Lett. 48, e2021GL094183 (2021).
- 20. Epstein, Y. & Moran, D. S. Thermal comfort and the heat stress indices. *Ind. Health* **44**, 388–398 (2006).
- Buzan, J., Oleson, K. & Huber, M. Implementation and comparison of a suite of heat stress metrics within the Community Land Model version 4.5. Geosci. Model Dev. 8, 151–170 (2015).
- Romps, D. M. & Lu, Y.-C. Chronically underestimated: a reassessment of US heat waves using the extended heat index. *Environ. Res. Lett.* 17, 094017 (2022).
- Raymond, C., Singh, D. & Horton, R. Spatiotemporal patterns and synoptics of extreme wet-bulb temperature in the contiguous United States. J. Geophys. Res. Atmos. 122, 13–108 (2017).
- Monteiro, J. M. & Caballero, R. Characterization of extreme wet-bulb temperature events in southern Pakistan. *Geophys. Res. Lett.* 46, 10659–10668 (2019).
- Zhang, Y., Held, I. & Fueglistaler, S. Projections of tropical heat stress constrained by atmospheric dynamics. *Nat. Geosci.* 14, 133–137 (2021).
- Chu, H. et al. The land wet-bulb temperature increases faster than the sea surface temperature. Geophys. Res. Lett. 51, e2023GL106617 (2024).
- Eltahir, E. A. & Pal, J. S. Relationship between surface conditions and subsequent rainfall in convective storms. *J. Geophys. Res.* Atmos. 101, 26237–26245 (1996).
- Sherwood, S. C. How important is humidity in heat stress?
 J. Geophys. Res. Atmos. 123, 11–808 (2018).
- Raymond, C. et al. On the controlling factors for globally extreme humid heat. Geophys. Res. Lett. 48, e2021GL096082 (2021).
- 30. Arakawa, A. & Schubert, W. H. Interaction of a cumulus cloud ensemble with the large-scale environment, Part I. *J. Atmos. Sci.* **31**, 674–701 (1974).
- 31. Emanuel, K. A., Neelin, J. D. & Bretherton, C. S. On large-scale circulations in convecting atmospheres. Q. J. R. Meteorol. Soc. **120**, 1111–1143 (1994).
- 32. Raymond, D. J. Regulation of moist convection over the west Pacific warm pool. *J. Atmos. Sci.* **52**, 3945–3959 (1995).
- 33. Neelin, J. D. & Zeng, N. A quasi-equilibrium tropical circulation model—formulation. *J. Atmos. Sci.* **57**, 1741–1766 (2000).
- Williams, I. N., Pierrehumbert, R. T. & Huber, M. Global warming, convective threshold and false thermostats. *Geophys. Res. Lett.* 36, L21805 (2009).

- Byrne, M. P. & O'Gorman, P. A. Land-ocean warming contrast over a wide range of climates: convective quasi-equilibrium theory and idealized simulations. J. Clim. 26, 4000–4016 (2013).
- Zhang, Y. & Fueglistaler, S. How tropical convection couples high moist static energy over land and ocean. *Geophys. Res. Lett.* 47, e2019GL086387 (2020).
- Byrne, M. P. Amplified warming of extreme temperatures over tropical land. Nat. Geosci. 14, 837–841 (2021).
- Zhang, Y. & Boos, W. R. An upper bound for extreme temperatures over midlatitude land. *Proc. Natl Acad. Sci. USA* 120, e2215278120 (2023).
- Duan, S. Q., McKinnon, K. A. & Simpson, I. R. Two perspectives on amplified warming over tropical land examined in CMIP6 models. *J. Clim.* https://doi.org/10.1175/JCLI-D-22-0955.1 (2024).
- Sobel, A. H. & Bretherton, C. S. Modeling tropical precipitation in a single column. J. Clim. 13, 4378–4392 (2000).
- Brown, R. G. & Zhang, C. Variability of midtropospheric moisture and its effect on cloud-top height distribution during TOGA COARE. J. Atmos. Sci. 54, 2760–2774 (1997).
- Sherwood, S. C., Minnis, P. & McGill, M. Deep convective cloud-top heights and their thermodynamic control during CRYSTAL-FACE. J. Geophys. Res. Atmos. 109, D20119 (2004).
- Holloway, C. E. & Neelin, J. D. Moisture vertical structure, column water vapor, and tropical deep convection. *J. Atmos. Sci.* 66, 1665–1683 (2009).
- 44. Schiro, K. A., Ahmed, F., Giangrande, S. E. & Neelin, J. D. GoAmazon2014/5 campaign points to deep-inflow approach to deep convection across scales. *Proc. Natl Acad. Sci.* **115**, 4577–4582 (2018).
- Raymond, C., Matthews, T. & Horton, R. M. The emergence of heat and humidity too severe for human tolerance. Sci. Adv. 6, eaaw1838 (2020).
- Ahmed, F. & Neelin, J. D. Reverse engineering the tropical precipitation-buoyancy relationship. J. Atmos. Sci. 75, 1587–1608 (2018).
- Ahmed, F., Adames, Á. F. & Neelin, J. D. Deep convective adjustment of temperature and moisture. *J. Atmos. Sci.* 77, 2163–2186 (2020).
- Ahmed, F. & Neelin, J. D. A process-oriented diagnostic to assess precipitation-thermodynamic relations and application to CMIP6 models. Geophys. Res. Lett. 48, e2021GL094108 (2021).
- Schiro, K. A. & Neelin, J. D. Deep convective organization, moisture vertical structure, and convective transition using deep-inflow mixing. J. Atmos. Sci. 76, 965–987 (2019).
- Neale, R. B. et al. Description of the NCAR community atmosphere model (CAM 5.0). NCAR Tech. 1, 1–12 (2010).
- Tyrlis, E., Lelieveld, J. & Steil, B. The summer circulation over the eastern Mediterranean and the Middle East: influence of the South Asian monsoon. Clim. Dyn. 40, 1103–1123 (2013).
- 52. Eyring, V. et al. Overview of the Coupled Model Intercomparison Project Phase 6 (CMIP6) experimental design and organization. *Geosci. Model Dev.* **9**, 1937–1958 (2016).
- 53. Danabasoglu, G. et al. The community earth system model version 2 (CESM2). J. Adv. Model. Earth Syst. 12, e2019MS001916 (2020).
- 54. Held, I. M. & Soden, B. J. Robust responses of the hydrological cycle to global warming. *J. Clim.* **19**, 5686–5699 (2006).

- 55. O'Gorman, P. & Muller, C. J. How closely do changes in surface and column water vapor follow Clausius-Clapeyron scaling in climate change simulations? *Environ. Res. Lett.* **5**, 025207 (2010).
- 56. Matthews, T. Humid heat and climate change. *Prog. Phys. Geo. Earth Environ.* **42**, 391–405 (2018).
- Lutsko, N. J. The relative contributions of temperature and moisture to heat stress changes under warming. J. Clim. 34, 901–917 (2021).
- 58. Byrne, M. P. & O'Gorman, P. A. Trends in continental temperature and humidity directly linked to ocean warming. *Proc. Natl Acad. Sci. USA* 201722312 (2018).
- Chou, C. & Neelin, J. D. Mechanisms of global warming impacts on regional tropical precipitation. J. Clim. 17, 2688–2701 (2004).
- Vecellio, D. J., Wolf, S. T., Cottle, R. M. & Kenney, W. L. Evaluating the 35°C wet-bulb temperature adaptability threshold for young, healthy subjects (PSU HEAT Project). J. Appl. Physiol. 132, 340–345 (2022).
- 61. Wolf, S. T., Cottle, R. M., Vecellio, D. J. & Kenney, W. L. Critical environmental limits for young, healthy adults (PSU Heat Project). *J. Appl. Physiol.* **132**, 327–333 (2022).
- Lu, Y.-C. & Romps, D. M. Extending the Heat Index. J. Appl. Meteorol. Climatol. 61, 1367–1383 (2022).
- 63. Vecellio, D. J., Kong, Q., Kenney, W. L. & Huber, M. Greatly enhanced risk to humans as a consequence of empirically determined lower moist heat stress tolerance. *Proc. Natl Acad. Sci. USA* **120**, e2305427120 (2023).
- 64. Lu, Y.-C. & Romps, D. M. Is a wet-bulb temperature of 35°C the correct threshold for human survivability? *Environ. Res. Lett.* **18**, 094021 (2023).
- 65. Emmenegger, T. et al. The physics behind precipitation onset bias in CMIP6 models: the pseudo-entrainment diagnostic and trade-offs between lapse rate and humidity. *J. Clim.* **37**, 2013–2033 (2024).
- Duan, S. Q., Wright, J. S. & Romps, D. M. On the utility (or futility) of using stable water isotopes to constrain the bulk properties of tropical convection. J. Adv. Model. Earth Syst. 10, 516–529 (2018).
- 67. Romps, D. M. A direct measure of entrainment. *Journal of the Atmospheric Sciences* **67**, 1908–1927 (2010).
- 68. Stevens, B. et al. DYAMOND: the DYnamics of the Atmospheric general circulation Modeled On Non-hydrostatic Domains. *Prog. Earth Planet. Sci.* **6**, 1–17 (2019).
- 69. Hersbach, H. et al. The ERA5 global reanalysis. Q. J. R. Meteorol. Soc. **146**, 1999–2049 (2020).

Publisher's note Springer Nature remains neutral with regard to jurisdictional claims in published maps and institutional affiliations.

Springer Nature or its licensor (e.g. a society or other partner) holds exclusive rights to this article under a publishing agreement with the author(s) or other rightsholder(s); author self-archiving of the accepted manuscript version of this article is solely governed by the terms of such publishing agreement and applicable law.

@ The Author(s), under exclusive licence to Springer Nature Limited 2024

Methods

Variables and measures

MSE. MSE is defined as MSE = $c_pT + L_vq + gz$, where c_p is the specific heat of dry air, T is the dry bulb temperature, L_v is the latent heat of vapourization, q is the specific humidity, g is the gravitational acceleration and z is the height above sea level. We calculate MSE at the reference level (2 m above the surface, MSE_{2m}) using T and q at the reference level, and the orographical height (using variable orog for models or surface geopotential for ERA5). In ERA5, dew-point temperature, dry-bulb temperature and surface pressure are used to calculate q at the reference level.

MSE'. Saturated MSE is defined as MSE' = $c_pT + L_pq^* + gz$, where q^* is the saturated specific humidity. We use all variables at the 500 hPa pressure level to calculate the 500 hPa MSE' (MSE $_{500}^*$). q^* is calculated using the MetPy $_{70}^{70}$ package with temperature and pressure as input variables.

Subsat. Subsaturatation is defined as the saturation deficit: subsat = $L_v(q - q^*)$. We calculate the 850 hPa subsaturatation (Subsat₈₅₀) using all variables at the 850 hPa pressure level.

The boundary-layer instability measure. The boundary-layer instability measure is defined as $\mathsf{MSE}_{2m} - (\mathsf{MSE}_{500}^*)_{\mathsf{ZM}}$ that is, the exceedance of MSE_{2m} to the constraint $(\mathsf{MSE}_{500}^*)_{\mathsf{ZM}}$ set by idealized theories of QE and WTG. $(\mathsf{MSE}_{500}^*)_{\mathsf{ZM}}$ is the zonal-mean value of MSE_{500}^* . From idealized QE, local MSE_{2m}^* is constrained by local MSE_{500}^* to remain neutrally buoyant. From WTG, anomalies of MSE_{500}^* are rapidly reduced by gravity waves, and the tropics thus maintains a relatively horizontally homogeneous MSE_{500}^* (set by high local MSE_{500}^*). Combining the two, $(\mathsf{MSE}_{500}^*)_{\mathsf{ZM}}$ gives a limit to local MSE_{2m}^* . Boundary-layer air exceeding this limit will be unstable. QE and WTG hold best in the deep tropics (roughly 20°S–20°N). Here, we examine 30°S–30°N to cover more subtropical area with a large population. A sensitivity test that only includes grid cells within 20^*S-20^*N is shown in Extended Data Fig. 5.

The LFT dryness measure. The LFT dryness measure is defined as wSubsat₈₅₀ – (MSE $_{500}^*$), where (MSE $_{500}^*$) is the deviation of local MSE $_{500}^*$ from $(MSE_{500}^*)_{ZM}$. Under entraining QE, to remain stable or neutrally buoyant, MSE_{2m} + entrainment effect stays neutral to MSE_{500}^* . We use wSubsat₈₅₀ to represent the entrainment effect of LFT dry air incorporated into convective plumes; with empirically equal weight to boundary-layer air⁴⁶, $w \approx 1$. Thus, $MSE_{2m} + Subsat_{850} \leq MSE_{500}^*$ (here Subsat₈₅₀ keeps its sign and is negative). To write the constraint in a variant form and incorporating deviations from WTG, we have $MSE_{2m} - MSE_{500}^* = MSE_{2m} - ((MSE_{500}^*)_{7M} + (MSE_{500}^*)') \le -Subsat_{850}There$ fore, $MSE_{2m} - (MSE_{500}^*)_{ZM} \le -(Subsat_{850} - (MSE_{500}^*)')$. Under idealized QE-WTG, $MSE_{2m} - (MSE_{500}^*)_{7M} \le 0$, whereas under entraining QE-WTG, a certain amount of LFT dry air effects (Subsat₈₅₀ – (MSE $_{500}^*$) allows for a certain amount of boundary-layer instability (MSE_{2m} – (MSE $_{500}^*$)_{7M}). In the LFT dryness measure, (MSE₅₀₀) is small and Subsat₈₅₀ is the dominant term. A sensitivity test where we do not include deviations from WTG is shown in Extended Data Fig. 6.

WBT. We calculate WBT using the Davies-Jones method 21,71 . We have also calculated WBT using the MetPy package as a cross validation, and the two methods yield very similar results (Extended Data Fig. 7). In the main text, we present those from the Davies-Jones method. When using the Davies-Jones method, input variables include T, q and surface pressure; when using MetPy, input variables include T, surface pressure and the dew point.

Data and experiments

ERA5. Hourly $0.25^{\circ} \times 0.25^{\circ}$ ERA5 (ref. 69) data were regridded into $1^{\circ} \times 1^{\circ}$ resolution and averaged into daily mean values before further analysis. We used data during 1980–1989, and consider the warm season since

it is the period most susceptible to extreme moist heat events. The warm season is defined as the 150 days centred on 15 and 16 July for the Northern Hemisphere and the 150 days centred on 15 and 16 January for the Southern Hemisphere.

Climate model outputs. We analyse simulations submitted to the CMIP6 (ref. 52). We take the first 30 years (1850–1879) in the historical experiment as the base climate state, and years 121–150 in the abrupt $4\times$ CO $_2$ experiment as the $4\times$ CO $_2$ climate state. We use 20 years for CESM2 due to a break of available output during 141–150 for selected three-dimensional daily variables. We use the output from six models that have reported daily values of all variables we need for both the historical and $4\times$ CO $_2$ experiments. The six models are: CanESM5, CESM2, GFDL-CM4, IPSL-CM6A-LR, MIROC6 and MPI-ESM1-2-HR. The limitation to these specific six models mainly comes from the availability of daily three-dimensional variables in the $4\times$ CO $_2$ experiment. We use the abrupt $4\times$ CO $_2$ for its clarity of the forcing and large amplitude of the warming signal to serve our purpose. The results are analysed for the warm season.

CAM5 experiments. We use two sets of CAM5 runs following ref. 48, where the entrainment rate (specifically the parcel fractional mass entrainment rate, i.e. the parameter dmpdz in CAM5) (ref. 72) is specified to be 0 km^{-1} (non-entraining) and 1 km^{-1} (default value in CAM5). For each experiment, the model is run with sea surface temperature and greenhouse gas concentrations fixed at the year 2000 value. The model is allowed to spin-up for 1 year. Three hourly data from the subsequent year during the warm season is used for analysis.

Sampling

ERA5. We use the land-sea mask file and categorize grid cells with land area fraction greater than 95% as land grid cells, less than 5% as ocean grid cells and those in between as coast grid cells. The top 1% days in Fig. 1 are sampled from all days and all grid cells over land, ocean and coast, respectively. We conduct sampling over land, ocean and coast separately because we are interested in whether there are systematic differences between land and ocean (and/or a mix of the two, that is, the coast) in conditions that produce extreme moist heat. In generating the two-dimensional joint distribution of the boundary-layer instability measure $(MSE_{2m} - (MSE_{500}^*)_{ZM})$ and the LFT dryness measure (Subsat₈₅₀ – (MSE $_{500}^*$)), we separately sample days with $P \ge 6$ mm per day (raining days) and days with $P \ge 0.5$ mm per day (non-raining days), and respectively aggregate land plus coast grid cells and ocean grid cells. The total number of samples as days × grid cells for land, ocean and coast is shown in Extended Data Fig. 8. Raining days constitute 20–30% and non-raining days constitute 30–40% of the total. Then, for samples over land plus coast and over ocean, we respectively divide their ranges (minimum minus 0.5 kJ kg⁻¹ and maximum plus 0.5 kJ kg⁻¹) of the two measures into 100 portions. For land plus coast, the range of the boundary-layer instability measure is -32.68 to 43.04 kJ kg⁻¹ and the bin size is 0.76 kJ kg⁻¹; the range of the LFT dryness measure is $(-126.01 \text{ to } 15.42 \text{ kJ kg}^{-1})$, and the bin size is 1.43 kJ kg⁻¹. For ocean, the range of the boundary-layer instability measure is -29.44 to 39.84 kJ kg⁻¹ and the bin size is 0.70 kJ kg⁻¹; and the range of the LFT dryness measure is -108.14 to 19.66 kJ kg⁻¹) and the bin size is 1.29 kJ kg⁻¹.

For Fig. 2, we calculate the frequency conditioned on the two measures in each bin for raining and non-raining days (in units of counts per bin, where counts is days \times grid cells), and then normalize the frequency by the total number of samples over land plus coast and over ocean, giving us the fractional frequency (in units of counts per counts per bin) which are plotted as the green and brown shadings. To reduce the overlap of the green shading on the brown one, we mask the lowest values at the edge of the green shading, while enforcing that 99% of the samples are kept and shown. Overlaid on the frequency distributions, we sample the top 1% WBT days over land plus coast (the top 1%

is sampled from the aggregated data of all days \times grid cells) and over ocean, and plot them as scatter dots (each dot represents one day) in Fig. 2a,b. For Fig. 3a,b, we plot the bin-averaged ω_{500} . Extended Data Fig. 9 in the Extended Data shows contours for absolute bin counts of 10 and 100 to provide a further sense of the statistical sampling.

CESM2. We use a similar sampling method as for ERA5. The total number of samples for land, ocean, and coast is shown in Extended Data Fig. 10. To generate the two-dimensional joint distribution of the boundary-layer instability measure and the LFT dryness measure, we divide the ranges (use the minimum between the control and the $4\times$ CO $_2$ experiment minus 0.5 kJ kg $^{-1}$, and the maximum between the control and the $4\times$ CO $_2$ experiment plus 0.5 kJ kg $^{-1}$) of the two measures into 100 portions. For land plus coast, the range of the boundary-layer instability measure is -40.71 to 53.25 kJ kg $^{-1}$) and the bin size is 0.95 kJ kg $^{-1}$; the range of the LFT dryness measure is -234.90 to 16.34 kJ kg $^{-1}$) and the bin size is 2.54 kJ kg $^{-1}$. For ocean, the range of the boundary-layer instability measure is -29.60 to 55.83 kJ kg $^{-1}$) and the bin size is 0.86 kJ kg $^{-1}$; and the range of the LFT dryness measure is -186.39 to 22.32 kJ kg $^{-1}$) and the bin size is 2.11 kJ kg $^{-1}$.

Multi-model mean. To generate the multi-model mean changes in the two-dimensional joint distribution in Fig. 5, we use the same set of bins for all models and for both the control and the $4\times$ CO $_2$ experiment: we divide the range of (-50 to 50 kJ kg $^{-1}$) into 150 portions and use them as bins for the boundary-layer instability measure, and we divide the range of (-200 to 20 kJ kg $^{-1}$) into 150 portions and use them as bins for the LFT dryness measure. We average the frequency distribution across models in each climate state before subtracting the frequency distribution of the control climate from that of the $4\times$ CO $_2$ climate. To provide a clear visualization, we mask the shading edge of the raining conditions that are in the lowest 1% cumulative frequency of the warm-climate joint frequency distribution.

Data availability

ERA5 hourly reanalysis data can be downloaded from the ECMWF Climate Data Store (https://cds.climate.copernicus.eu). CMIP6 model outputs used in this study can be downloaded from the CMIP6 data archive (https://esgf-node.llnl.gov/search/cmip6/). The CAM5 entrainment experiment data used for this study, and post-processed data underlying all figures, in both the main text and the extended data, have been deposited in Dryad (https://doi.org/10.5061/dryad.1ns1rn92v).

Code availability

A Python script to calculate the WBT with the Davies-Jones method can be found public at Dr. Xianxiang Li's Github repository (https://github.com/smartlixx/WetBulb). The MetPy package can be installed following guidance from its website (https://unidata.github.io/MetPy/

latest/index.html). Codes for conducting the analyses are available upon request.

References

- May, R. M. et al. MetPy: a meteorological Python library for data analysis and visualization. *Bull. Am. Meteorol. Soc.* 103, E2273–E2284 (2022).
- 71. Davies-Jones, R. An efficient and accurate method for computing the wet-bulb temperature along pseudoadiabats. *Mon. Weather Rev.* **136**, 2764–2785 (2008).
- 72. Neale, R. B., Richter, J. H. & Jochum, M. The impact of convection on ENSO: from a delayed oscillator to a series of events. *J. Clim.* **21**, 5904–5924 (2008).

Acknowledgements

The authors acknowledge support from Department of Energy Regional and Global Model Analysis award DE-SC0023244, National Science Foundation awards AGS-1936810 (S.Q.D., F.A. and J.D.N.) and AGS-2225956 (F.A.) and National Oceanic and Atmospheric Administration award NA210AR4310354 (S.Q.D., F.A. and J.D.N.). The authors appreciate European Centre for Medium-Range Weather Forecasts, climate modelling groups and the Earth System Grid Federation for producing, archiving and making available the ERA5 and CMIP6 model data.

Author contributions

All authors designed the study and contributed to the interpretation of results and writing of the manuscript. S.Q.D. conducted data analysis and visualization. The CAM5 entraining experiments were conducted by F.A.

Competing interests

The authors declare no competing interests.

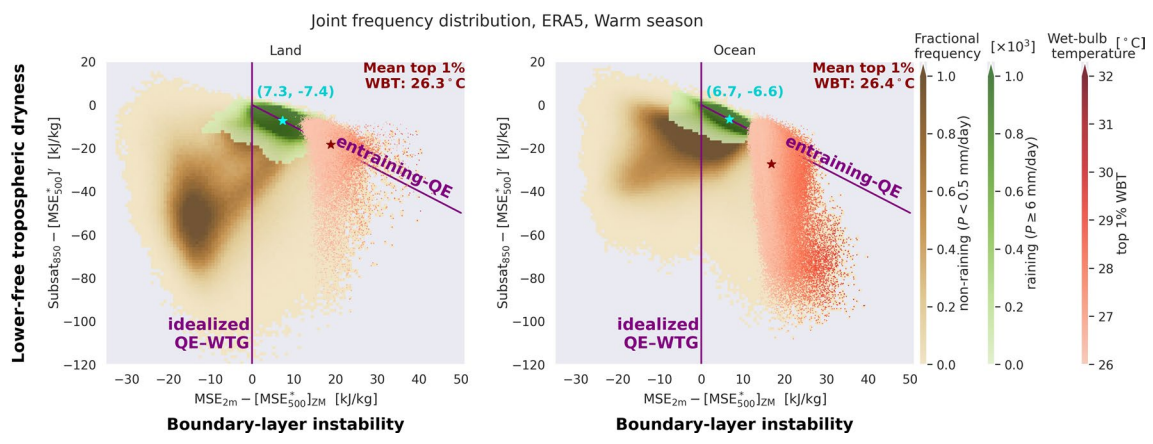
Additional information

Extended data is available for this paper at https://doi.org/10.1038/s41561-024-01498-y.

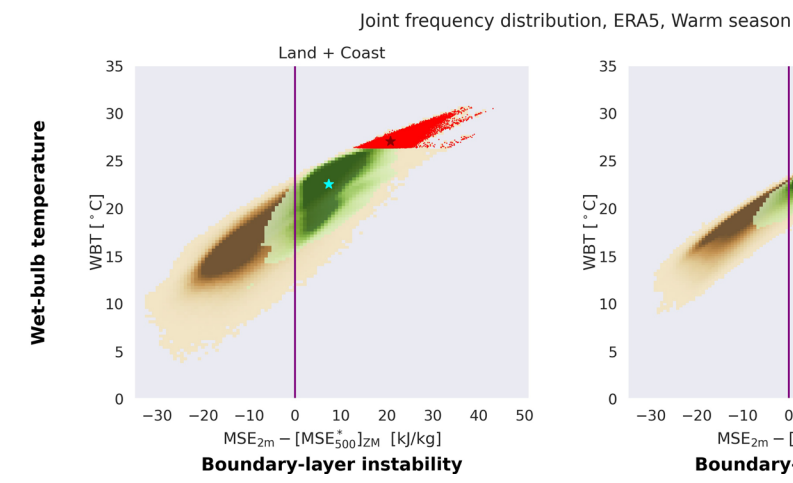
Correspondence and requests for materials should be addressed to Sugin Q. Duan.

Peer review information *Nature Geoscience* thanks Larissa Back, Colin Raymond and the other, anonymous, reviewer(s) for their contribution to the peer review of this work. Primary Handling Editor: Tom Richardson, in collaboration with the *Nature Geoscience* team.

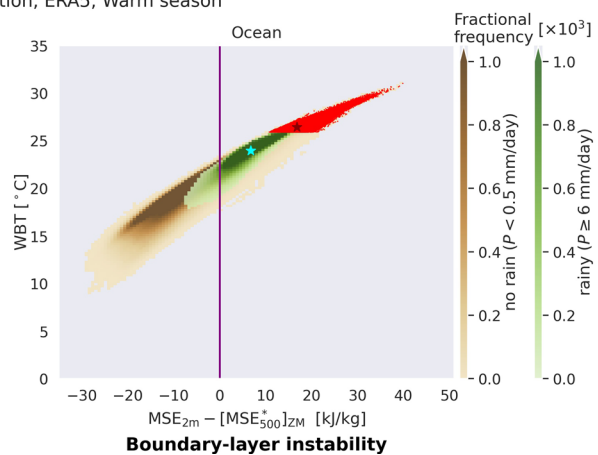
Reprints and permissions information is available at www.nature.com/reprints.



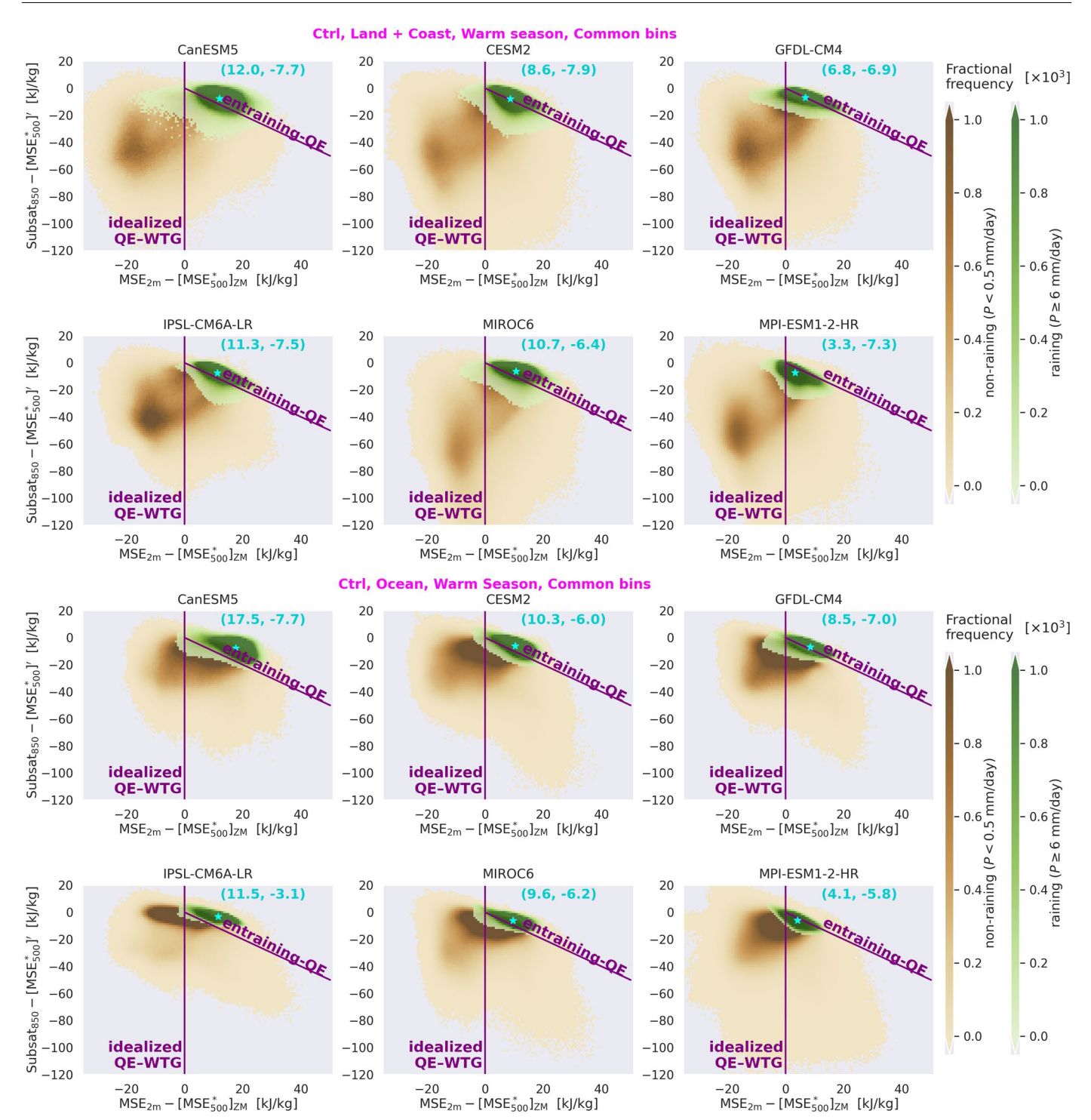
Extended Data Fig. 1 | The joint frequency distribution of the instability/dryness measures for land grid cells only. Similar to Fig. 2, but the left panel is based on days over land grid cells only. Fig. 2b is repeated in the right panel for reference.



Extended Data Fig. 2 | Mapping wet-bulb temperature values to the boundary-layer instability measure. An illustration of the correspondence of wet-bulb temperature (WBT) values to the BL instability: frequency of non-raining (daily mean precipitation rate P < 0.5 mm/day; brown shadings) and raining ($P \ge 6 \text{ mm/day}$; green shadings) conditions, and the top 1% wet bulb

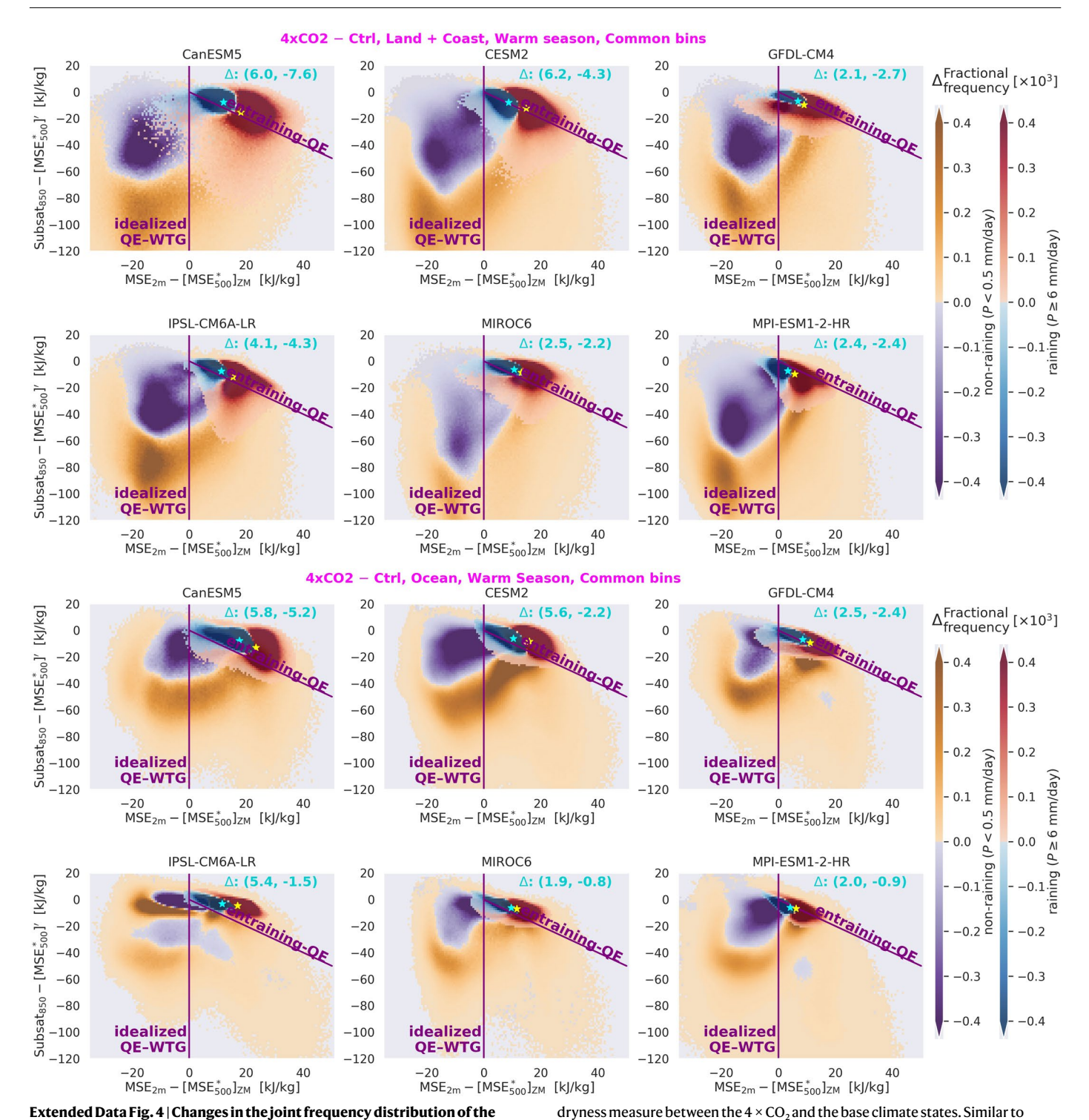


temperature days (red dots), as a function of the boundary-layer instability and wet-bulb temperature, for (a) land plus coast, and (b) ocean in ERA5. The cyan stars show the mean for raining conditions, and the dark red stars show the mean for the top 1% WBT days.



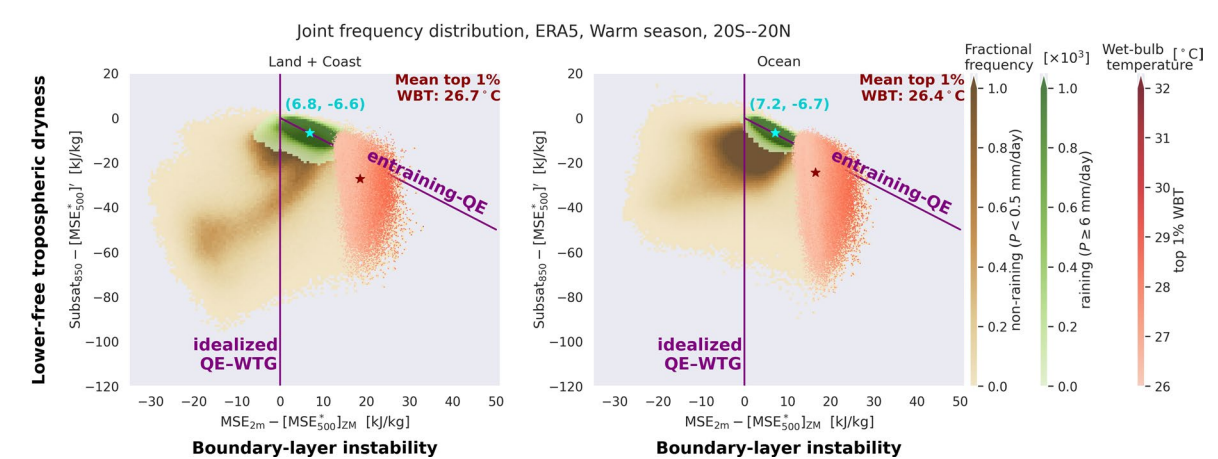
Extended Data Fig. 3 | The joint frequency distribution of the instability/dryness measures in individual climate models. Frequency of raining/non-raining conditions (green/drown shading) as a function of the boundary-layer instability measure and the lower-free tropospheric (LFT)

dryness measure, similar to Fig. 2 but for the base climate in individual models. The first six panels show the distribution for land plus coast, and the latter six panels show the distribution for ocean.



instability/dryness measures between the warm and the base climate states in individual climate models. Changes in the joint frequency distribution of the boundary-layer instability measure and the lower-free tropospheric (LFT)

dryness measure between the $4\times CO_2$ and the base climate states. Similar to Fig. 5a–b but for individual models. The first six panels show the distribution for land plus coast, and the latter six panels show the distribution for ocean.

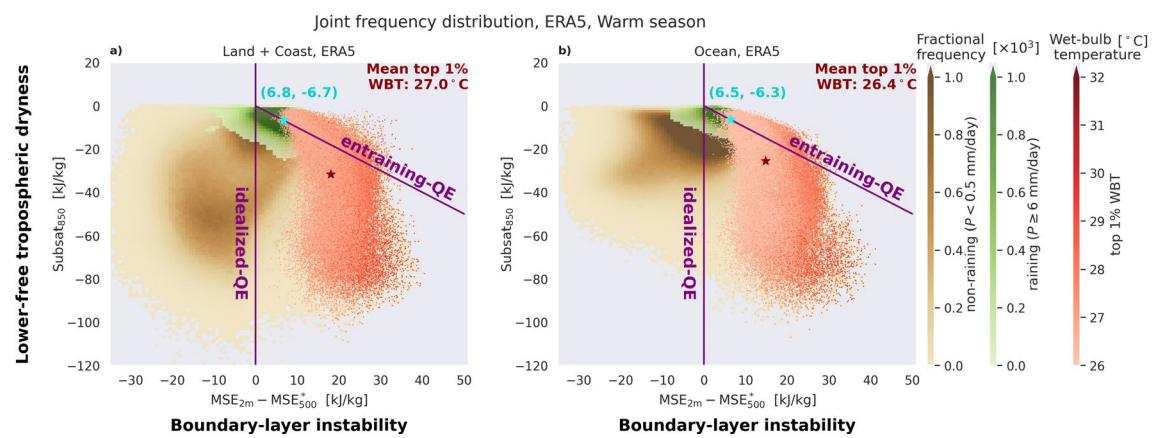


Extended Data Fig. 5 | **The joint frequency distribution of the instability/ dryness measures when only grid cells within 20°S–20°N are included.** Sensitivity test (see Methods M1) for comparison to Fig. 2a–b, but only including grid cells within 20°S–20°N. The frequency distributions show generally similar patterns: raining samples align along the entraining QE line and a large number of non-raining samples exceeding the idealized QE–WTG limit form the dry-inhibition regime. The dry-inhibition regime extends slightly less far towards

very subsaturated LFT, that is, the most subsaturated points occur outside

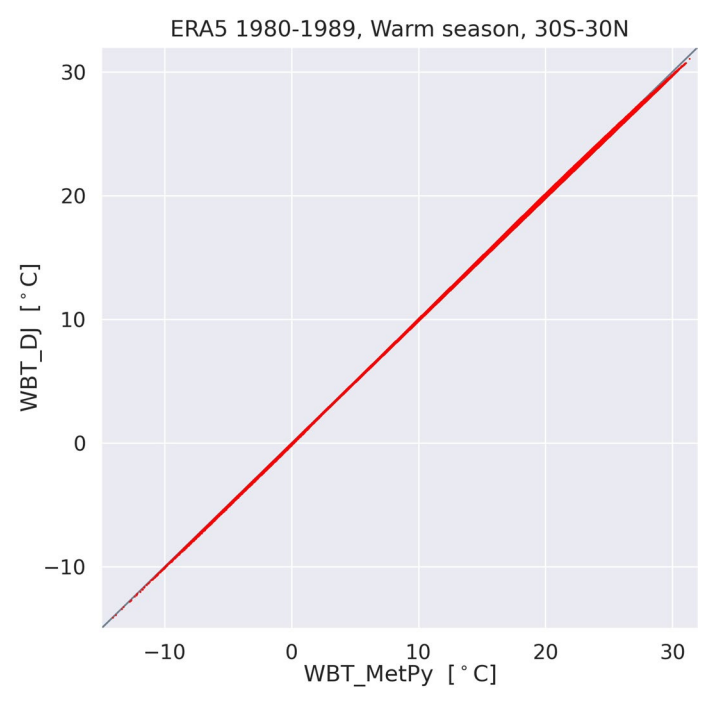
 $20^\circ\text{S}-20^\circ\text{N}$. For land plus coast, a density center on the stable (left) side of the idealized QE–WTG limit is weaker in this figure since many of those conditions are over the subtropical desert. As in Fig. 2, the top 1% wet-bulb temperature days occur at the highest values of the BL instability measure and are distributed in

both the convective and the dry-inhibition regimes. The similar patterns confirm that the behavior regimes we show in the main text are robust to the inclusion of subtropical latitudes 20-30°S and N.

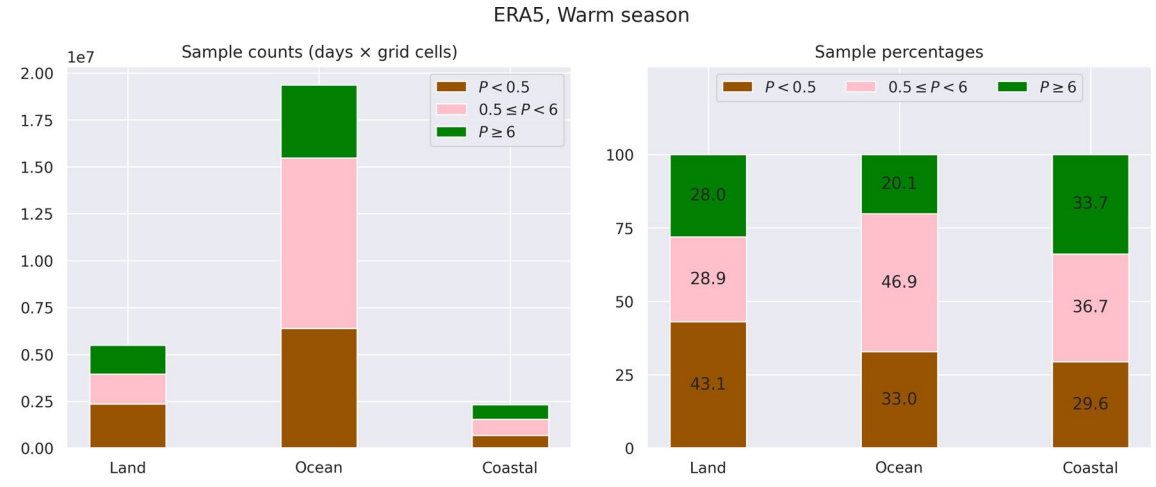


Extended Data Fig. 6 | The joint frequency distribution of the instability/dryness measures when not considering the weak temperature gradient (WTG) component. Sensitivity test (see Methods M1) for comparison to Fig. 2a-b, but without including the WTG component. When not considering WTG, Subsat $_{850}$ compensates for the excessive MSE $_{2m}$ to the local column MSE $_{500}^*$

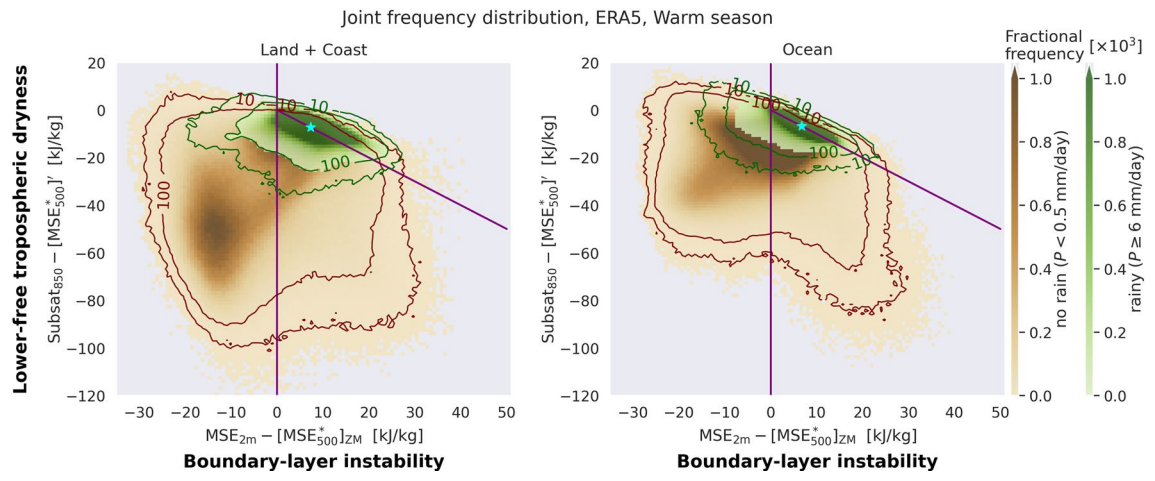
to maintain convective neutrality. The frequency distributions in this figure (\mathbf{a} , land plus coast; \mathbf{b} , ocean) show similar patterns compared with Fig. 2a,b, indicating that deviations from WTG play a minor role compared with the LFT entrainment effect in explaining samples exceeding the idealized QE constraint.



 $\textbf{Extended Data Fig. 7} | \textbf{Cross validation of wet-bulb temperatures calculated by two methods.} \ A \ comparison of wet bulb temperatures (WBTs) \ calculated using the Davies-Jones method (WBT_DJ) versus the MetPy package (WBT_MetPy). Each dot represents one day at one grid cell during 1980–1989 warm season in ERA5. The gray line shows the 1:1 for reference.$



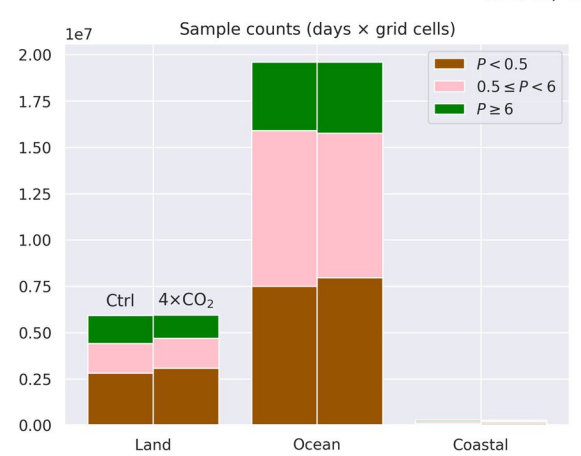
 $\textbf{Extended Data Fig. 8} | \textbf{An overview of samples used from the ERA5 reanalysis data.} \ O \textit{verview of sample counts} \ (left panel) \ and \ percentages \ (right panel) for different categories of precipitation rate over land, ocean and coast in ERA5. The total sample pool for each bar consists of 10 years \times 150 warm-season days/year \times the number of land, ocean and coast grid cells.$



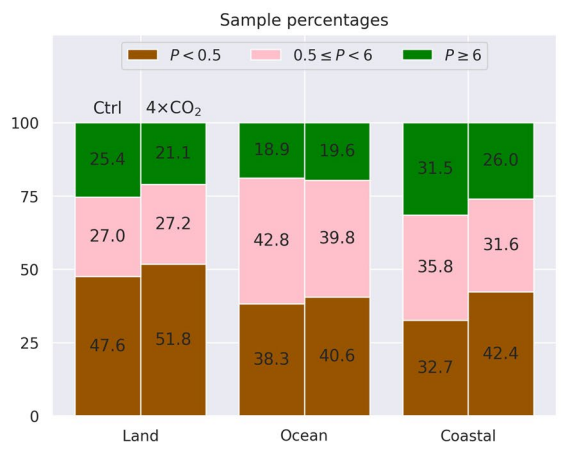
Extended Data Fig. 9 | The absolute sample counts for the frequency distribution of the instability/dryness measures. The same frequency distributions as in Fig. 2a–b, but with two contours marking the absolute counts 10 and 100 in each bin for raining and non-raining conditions respectively.

The edges of the frequency distribution with the lowest count values for raining conditions (green shadings) are masked for sake of clear visualization; the unmasked distribution cover 99% of the raining samples.

CESM2, Warm season



Extended Data Fig. 10 | **An overview of samples used from the CESM2 model data.** Overview of sample counts (left panel) and percentages (right panel) for different categories of precipitation rate over land, ocean and coast in CESM2



for the control and the $4 \times CO_2$ experiments. The total sample pool for each bar consists of 10 years \times 150 warm-season days/year \times the number of land, ocean and coast grid cells.